Materialia 26 (2022) 101578

Contents lists available at ScienceDirect

Materialia

journal homepage: www.elsevier.com/locate/mtla

High-fidelity Modeling and Validation of Electrohydrodynamic Jet Printing

Nazanin Farjam*, Isaac A. Spiegel, Kira Barton

Department of Mechanical Engineering, University of Michigan, 2505 Hayward St, Ann Arbor, MI 48109, United States

ARTICLE INFO

MSC:
0000
1111
Micro-additive manufacturing
E-jet printing
Physics-based modeling
Leaky-dielectric
Material characterization

PACS:
0000
1111

ABSTRACT

High-resolution electrohydrodynamic jet (e-jet) printing has provided a new route to flexible fabrication design of electronic devices. However, there are gaps in understanding this novel micro-additive manufacturing (μ-AM) process and the key material parameters that dictate the material jetting behavior. This paper provides a framework for high-fidelity modeling of drop-on-demand high-resolution e-jet printing that addresses this knowledge gap, which currently leads to slow and costly process optimization through experimental testing. The model is implemented in COMSOL Multiphysics and based on the leaky-dielectric model for an applied pulsed voltage, where the level set method is used to track the ink-air interface. The simulation results successfully demonstrate the critical process steps including equilibrium, Taylor Cone formation, the creation of a jet, jet break, and material retraction to the nozzle. The model is validated using high-speed printing images that are taken from a similar experimental setup. Four different case studies are conducted using the simulation model to investigate the impacts of key material parameters including viscosity, surface tension, electrical conductivity, and relative permittivity on the e-jet process, where it is shown in simulation that viscosity, surface tension and electrical conductivity have a higher impact on jetting frequency and deposited droplet volume.

1. Introduction

Additive manufacturing (AM) is in a steady growth trajectory due to its advantages such as flexible designs, lower resource requirements, and faster production rates over many traditional manufacturing technologies. To truly harness the benefits from AM, there is a need for a better understanding of the AM process behavior and how material parameters play a role in these process dynamics outside of costly experimental testing. Simulation environments have often served as a proxy for experimental demonstration. There exist many different types of modeling and simulation environments and among them, high-fidelity models provide more complete knowledge about the complicated physics behind AM system processes [1–3]. Moreover, these models create a framework for an accurate prediction of the process dynamics resulting from the selection of process parameters and material properties [4–6]. These predictions provide insights into how to optimize the process parameters and material selections to achieve the desired printed device functionality based on requirements for product applications [7]. In spite of these important advancements driven by high-fidelity modeling, the current literature lacks complete high-fidelity models for many micro-additive manufacturing processes (μ-AM), such as near-field electrohydrodynamic jet (e-jet) printing [8], due to the complex physics and challenges in model validation that stem from the high-speed, high-resolution dynamics.

E-jet printing is a high-resolution jet-based micro additive manufacturing process that uses an electric potential between an ink-filled conductive micro-capillary nozzle and a grounded substrate to pull ink material out of the nozzle. Once the material is pulled out of the nozzle, the applied electric field induces an ejection process in which the ink becomes a continuous jet moving towards the substrate. This electrohydrodynamic induced technique is capable of printing high-resolution patterns (50 nm–50 μm) using a wide range of ink material selections (viscosities up to 10^5 cP), resulting in many novel applications, [9,10]. Example applications that use e-jet printing for fabrication include transparent glass heaters (TGHs) [11] and flexible transparent electrodes (FTEs) [12] that incorporate high-resolution embedded metal meshes offering excellent optoelectronic performance.

The functional performance of an e-jet printed pattern depends on the ejection behavior of the ink as well as the spreading and coalescence behavior of the ink on the substrate [13]. Much of the existing work in the e-jet modeling literature has focused on studying the initial jetting dynamics [14–17] or the material spreading and coalescence behavior on the substrate [13,18]. The work in this paper focuses on understanding the connection between material properties and the jetting dynamics captured from the initial jet formation, through the jetting process, to droplet impingement, and retraction from the substrate. Importantly, droplet coalescence behavior is not studied in this work, although the combination of the full jetting dynamics with droplet coalescence on the substrate will be considered as an important next step.

* Corresponding author.
E-mail address: nazanin.farjam@gmail.com (N. Farjam).

https://doi.org/10.1016/j.mtla.2022.101578
Received 13 June 2022; Accepted 13 September 2022
Available online 16 September 2022

Due to the complexity of e-jet physics, the majority of current modeling efforts for e-jet printing are based on scaling laws, where the authors propose relationships between process inputs, such as applied voltage and material characteristics, and process outputs, such as the jetting frequency or jet diameter [19–21]. While scaling laws provide guidelines for understanding simple and static relationships, they do not have the complexity or accuracy of high-fidelity models that can be used to predict material behavior.

Other e-jet literature focuses on the use of simplified physics to describe dynamics of a stable meniscus [14,15]. However, these initial frameworks are not able to describe the jetting behavior due to the complex capacitor geometry that exists during the jetting process, which cannot be described by first principle physics. Recent works combine first principles with data-driven models. In [16,17], the authors introduce a hybrid modeling framework that describes meniscus evolution using first-principles and jetting behavior using a purely date-driven model. The authors define this framework as a controls-based model suitable for control design and implementation. However, the data-driven component requires the extraction of model parameters from experimentation, which is expensive considering that these models are not scalable across nozzle size, offset height, or material classes.

There has been some work in the e-jet literature that includes high-fidelity modeling using a “leaky-dielectric” model to describe the electrohydrodynamics phenomenon [22,23]. While majority of this work studied electrohydrodynamic atomization and electrowetting, e.g. [24,25], there are other works that focused on the simulation of a large scale (low-resolution) e-jet process using multi-physics commercial tools, e.g. [26–28]. These works focused on the development of high-fidelity models for low-resolution e-jet printing (nozzle opening sizes greater than 100 μm and standoff heights above 500 μm), which do not scale to the high-resolution e-jet process due to the differences in the impact of specific forces such as gravity (low resolution) and capillary forces (high resolution) on the specific process dynamics. Singh et al. [29] focused on a high-resolution e-jet printing process for nozzle sizes of 2 and 10 μm with a standoff height of 100 μm. However, this work neglected capillary forces at the nozzle wall, which play an important role given the nozzle sizes used in high-resolution e-jet printing. More importantly, the e-jet simulation provided in Singh and Subramanian [29] assumes a constant flow rate at the nozzle inlet that is invalid for high-resolution e-jet applications, where the flow rate is shown to be a function of applied voltage signal [17]. Recent work by the authors relaxed the assumption of constant flow rate and focused on the first two stages of the electrohydrodynamic (e-jet) jetting dynamics: meniscus deformation (build-up) and jetting initiation [30]. This model was based on electrostatics and required an assumption of a nonconductive material. In contrast, the work presented in this manuscript includes the addition of electric current physics and a relaxation of the nonconductive material assumption in order to capture all four phases of the jetting dynamics. The core contributions of this work include:

- Development of a high-fidelity e-jet model for a pulsed voltage that captures all four phases of the jetting dynamics: build-up, jetting, jet break and retraction. Additionally, this work discusses the limitations of modeling only the first two stages and the potential uses of our proposed model for accurate drop-on-demand printing studies.
- In addition to the important extension to the theoretical foundations of the physics that drive the jetting dynamics and the implementation through a high-fidelity model, this manuscript includes experimental validation of the four stages of the jetting process. This validation includes high-speed images captured with a high-speed experimental set-up that provides an important model validation aspect that is missing in many e-jet modeling papers.
- This work provides a description of key metrics that should be evaluated to enable a quantitative analysis when comparing how different material properties of the ink lead to variations in both the jetting time and deposited droplet volume. This is an important contribution to demonstrate the effectiveness of the model for capturing ink material / process parameter relationships.

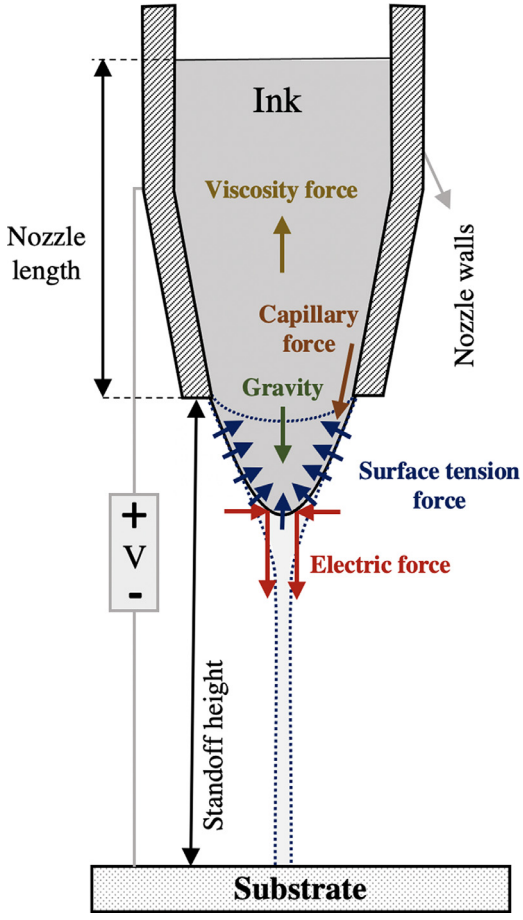

Fig. 1. Graphical description of the governing physics during the E-jet printing process.

This paper is organized as follows: Section 2 provides a background of the e-jet printing process and presents the governing physics that drive the process. The governing equations of the leaky-dielectric model, which provide the baseline for the presented framework, the model setup and the experimental setup are described in Section 3. Section 4 presents a comparison between the simulation and experimental results. This section also provides a sensitivity analysis of the key material parameters on jetting frequency and deposited droplet volume. Section 5 summarizes the presented work and identifies open areas for future research.

2. Electrohydrodynamic jet printing process

The standard high-resolution e-jet printing setup is depicted in Fig. 1, where a voltage is applied between an emitter i.e. a conductive micro-capillary nozzle filled with a polarizable ink material and an extractor i.e. a grounded conductive substrate. The electric field generated by the distribution between the nozzle and the substrate deforms the meniscus into a sharp tip (“Taylor cone”) that extends toward the grounded substrate. As the applied electric field force surpasses the surface tension within the nozzle, the ink will break from the nozzle and form a continuous jet from the nozzle to the substrate. After sufficient ions (and material) impinge and transfer to the substrate, the continuous jet will break and the meniscus will retract to its initial state until the next pulsation.

When applying a DC voltage to the nozzle, the pulsation is governed by a continuous jetting cycle (meniscus generation to break-off) often termed the natural dynamics of the process. A constant DC applied voltage ensures that charge transport between the fluid and substrate results in a continuous cycle of the 4-stages of the jetting process. On the other hand, a pulsed voltage includes a low voltage, where the meniscus is at equilibrium, a high voltage, which creates enough electric field to result in jetting, and a pulse duration, which is less than the required time for the natural jet break (so-called "subcritical regime"). It should be noted that the volume of ink deposited on the substrate is determined by the design of the applied voltage signal. In this paper, we apply a pulsed voltage signal in which the pulse width determines the amount of ink released during the printing process. For example, if the pulse width is large, multiple jetting episodes (repetition of formation, ejection, and retraction) will occur at a single location resulting in a larger overall volume of material deposited in one place. A pulsed voltage signal will result in a drop-on-demand process mode, where the process cycle is controllable and robust. To ensure a controllable printing mode, we have focused on a pulsed voltage signal in this work.

The e-jet printing process leverages a liquid jet pulsation induced by electrohydrodynamics, where there exists two categories of forces applied to the meniscus. One category includes the forces that oppose the jetting and fluid flow towards the substrate such as viscosity and surface tension forces, while the second category consists of the forces that contribute to the jetting process including gravity and the electric force. Depending on the ink material interactions with the nozzle wall, detailed in Section 3, capillary forces due to the ink wetting behavior on the nozzle wall sit either in the first or the second category. The e-jet phenomenon can be defined by three main governing physics:

- Fluid motion: governed by Navier–Stokes equations for viscous fluids; external forces include gravity (F_g), electric force (F_E), surface tension (F_γ), and the capillary force along the nozzle wall (F_{wall})
- Electric field distribution between the emitter (nozzle) and the extractor (substrate): governed by Gauss's law coupled with charge conservation equation; results in the generation of an electric charge at the ink-air interface and creation of an external force (F_E) to the meniscus
- Ink-air interface dynamics: governed by two-phase flow physics; defines two external forces applied to the meniscus: surface tension (F_γ) and capillary forces at the nozzle wall (F_{wall})

3. Methods

3.1. Governing equations

In this section, we provide the governing equations for the three physics-based interfaces that define the electrohydrodynamic phenomenon during e-jet printing: laminar flow to explain the fluid motion, electric currents to account for the electric field distribution, and the level set method to track the ink-air interface. The governing equations for each interface and their coupling are depicted in Fig. 2.

Laminar flow Laminar flow of an incompressible fluid can be described by the Navier–Stokes and continuity equations (Fig. 2, Eqs. (1) and (2)) solving for the fluid velocity, u and pressure, p. ρ and μ are the material density and viscosity. ∇ and $\nabla\cdot$ stand for gradient and divergence operator, respectively. The Navier–Stokes equation comes from the conservation of momentum, where $\rho\frac{\partial u}{\partial t} + \rho(u\cdot\nabla)u$ is the inertial term, $-\nabla p$ is the pressure force, and $\nabla\cdot[\mu(\nabla u + (\nabla u)^T)]$ is the viscosity force. The external forces, F_{ext}, for the process include gravity, $F_g = \rho g$, where g denotes the gravity vector, electric force (F_E), surface tension (F_γ), and capillary force (F_{wall}).

Electric currents The second set of governing equations calculates the electric field distribution for leaky-dielectric materials using three coupled equations including, Gauss's law (Fig. 2, Eq. (3)), the relationship between electric field, E and electric potential, V (Fig. 2, Eq. (4)), and charge conservation equation (Fig. 2, Eq. (5)). ε, σ are the material relative permittivity and electrical conductivity. ρ_f indicates the charge density. The electric force (F_E) is calculated using Eq. (6) in Fig. 2, i.e. the divergence of the Maxwell stress tensor, T. While $\rho_f E$, in this equation indicates the Coulombic force as a result of the electric field and the charged interface interactions, $-\frac{1}{2}E^2\nabla\varepsilon$, is the force coming from the transition in the fluid relative permittivity along the ink-air interface.

Level set method To track the ink-air interface, we need to define a two-phase flow algorithm. The governing equations for fluid flow and electric field distribution, Eqs. (1)–(6) are used to describe the physics within each air or ink phase using constant material properties such as fluid density, viscosity, electrical conductivity and relative permittivity. However, the material properties at the ink-air interface transition from the ink to the air material properties smoothly. By tracking the ink-air interface, the material properties can be updated based on the two-phase tracking method. Researchers have used various approaches for tracking two-phase fluid interface including volume-of-fluid (VOF), Pan and Zeng [28], phase field, Zhao et al. [27], Singh and Subramanian [29], and level set method (LSM), Mohammadi et al. [26]. LSM is selected for the current work due to its accuracy and robustness in high-resolution surface curvature applications. The governing equation for interface evolution using LSM (Eq. (7) in Fig. 2) moves the ink-air interface with the velocity field, u. In this equation, the value of the level set function, ϕ goes smoothly from 0 (liquid phase) to 1 (air phase) along the ink-air interface. ϵ_{ls} and λ are the interface thickness parameter and the reinitialization parameter, which ensures that the variations of the level set function are contained within the interface thickness. Solving the level set Eq. (7) to determine ϕ, the material properties in Eqs. (8)–(11) can then be calculated and used in the governing equations within laminar flow and electric current segments.

The LSM is coupled with the laminar flow interface by two external forces that are applied to the meniscus; the first one is surface tension force, F_γ that acts on the ink-air interface. This force is calculated using Eq. (12) in Fig. 2, where $S = \gamma(I - (nn^T))\delta$. γ, n and δ denote surface tension coefficient, unit normal to the interface and a Dirac delta function with its value being nonzero only at the ink-air interface. The second external force is capillary force, F_{wall} acting on the ink material at the ink-air-nozzle wall interface, which is obtained by Eq. (13) in Fig. 2. The first term in this equation, $\delta\gamma(n_{wall}\cdot n - \cos\theta)n$ enforces the ink material contact angle with the nozzle wall, θ, while the second term, $\frac{\mu}{\beta}u$ is a frictional force. n_{wall} and β denote the wall normal and the slip length, respectively.

3.2. Model setup

To generate the simulation model used in this paper, we applied the following assumptions within this framework:

A1. Incompressible and laminar fluid flow within the jetting process.
A2. Axisymmetric jetting through the Taylor cone approximation.

These assumptions are applied to reduce the computational complexity and calculation time of the simulation. Assumption A1 enables the use of simplified Navier–Stokes and continuity equations for incompressible and laminar flows, i.e. Eqs. (1) and (2) in Fig. 2. Assumption A2 allows us to define the nozzle geometry in a 2D-axisymmetric domain (See Fig. 3) and cylindrical coordinates, significantly reducing simulation times. Due to A2, the model cannot capture 3D variations in the jetting dynamics. To capture behaviors such as multiple jets, whipping, or electric field interference in the case of multi nozzles, one would need to extend this work to a 3D form, requiring electric force equations to be written in 3D. Future research may look to extend into these domains to better understand how to control and mitigate these jetting behaviors.

The geometry of the model is defined as shown in Fig. 3 considering the dimensions of the setup. The material properties for ink and air materials that need to be identified or measured are viscosity, μ, den-

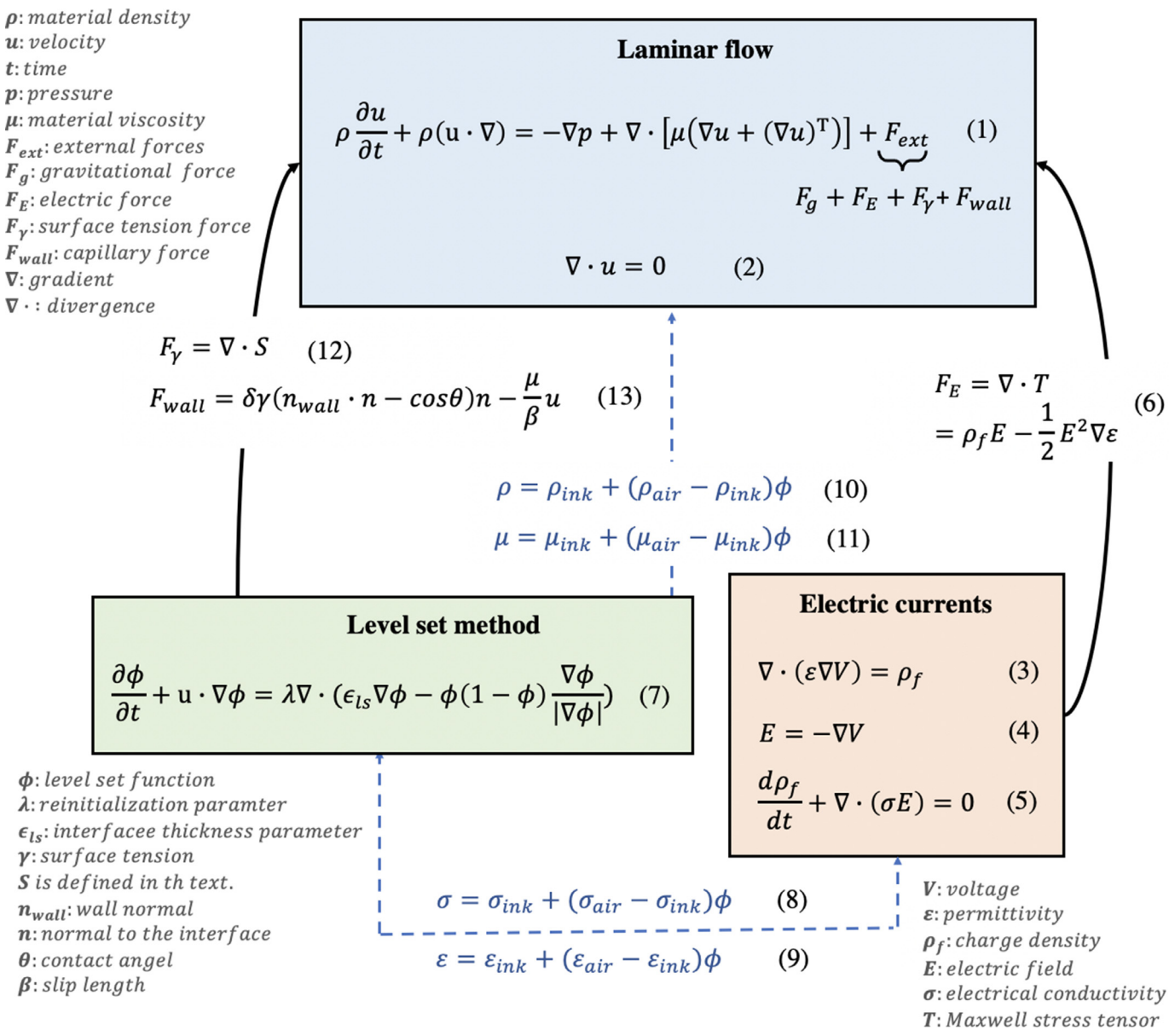

Fig. 2. Graphical description of the involved physics and the governing equations during the E-jet printing process.

sity, ρ, relative permittivity, ϵ, electrical conductivity, σ, surface tension coefficient, γ and contact angle on the nozzle wall, θ.

The boundary conditions and initial values for every domain are required to be defined for any computational physics problem. Therefore, we have provided Fig. 3 to specify the current model boundary conditions and initial values. The nozzle inlet boundary (Fig. 3, boundary b_1) is the ink material hydrostatic pressure, $P_0 = \rho g L$, where L is the nozzle length filled with the ink material. For the LSM physics, we define an inlet boundary condition of $\phi = 0$ to define the nozzle replenishing with the ink material at the inlet. While the electric force expression is added to the Navier–Stokes equation as a body force, the capillary force at the nozzle wall, F_{wall}, is added through a "wetted wall" boundary condition under the "multiphysics" module (Fig. 3, boundary b_2). This boundary condition, $u.n_{wall} = 0$ and F_{wall} enforce ink contact angle with the capillary inside wall, θ. The outside boundary (Fig. 3, boundary b_3) is defined as an outlet in the fluid physics, i.e. $p = 0$, and the substrate (Fig. 3, boundary b_4) is defined as a wall, i.e. $u = 0$. For the electric current interface, a pulsed electric potential boundary condition, with a baseline of V_l and a peak of V_h starting at $t = t_0$ and ending at $t = t_1$, is considered at the nozzle wall.

The initial conditions for the model setup include a meniscus in equilibrium i.e. an spherical cap shape for the initial interface and a low voltage applied to the ink material domain (D_1). Therefore, the initial values for the inner nozzle (D_1) and outside domain (D_2) are defined as a steady fluid, i.e. $p_{in} = 0$ and $v_{in} = 0$. The initial voltage (V_{in}) of D_1 is V_l, while that of the D_2 domain is 0. The initial phase defines ink material for D_1 and air material for D_2. After integrating the physics, boundary conditions and initial conditions to the model, a mesh needs to be defined for the simulation domain. Section 4. discusses the simulation results including model verification and sensitivity analysis of the material key parameters.

3.3. Experimental setup

Experiments are conducted using a custom-made e-jet printer in the Barton Research Group at the University of Michigan, see Fig. 4. This setup is composed of an X-Y-Z nanopositioning stage (Aerotech, "Planar$_{DL}$"), a vacuum chuck on top of the stage to hold the substrate in place, an in-house constructed nozzle holder, a voltage amplifier (TREK, 677B), a commercial high-speed camera (Vision Research, Phantom

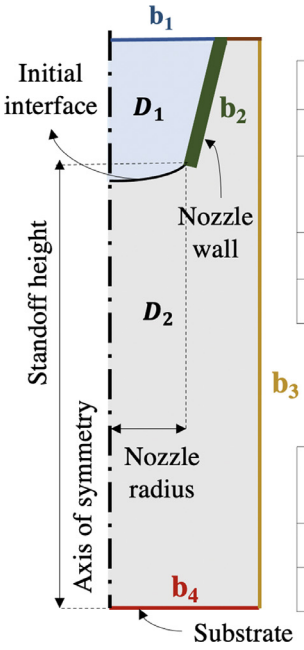

Model Boundary Conditions

Boundary	Laminar flow	Electric currents	LSM
b_1	$p = \rho g L$	$\rho_f = 0$	$\phi = 0$
b_2	$u.n_{wall} = 0$	$V = (V_h - V_l) * [H(t - t_0) - H(t - t_1)] + V_l$	N/A
b_3	$p = 0$	$\rho_f = 0$	N/A
b_4	$u = 0$	$V = 0$	N/A

Model Initial Values

Domain	Laminar flow	Electric currents	LSM
D_1	$p_{in}, v_{in} = 0$	$V_{in} = V_l$	$\phi = 0$
D_2	$p_{in}, v_{in} = 0$	$V_{in} = 0$	$\phi = 1$

p: pressure
v: velocity
V: voltage
ρ_f: charge density
ϕ: level set function
n_{wall}: wall normal
t: time
H: heaviside function

Fig. 3. Geometry of the model setup, boundary conditions and initial values. Subscript "in", "l" and "h" denote the initial value, low and high, respectively.

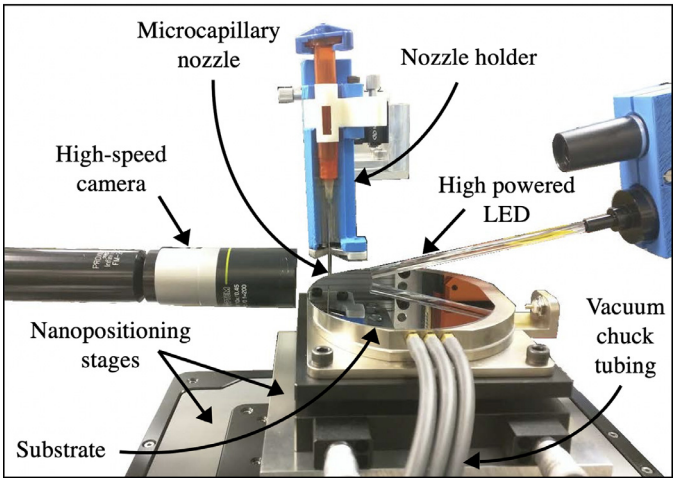

Fig. 4. Experimental setup used for model validation.

V9.0), and a high-powered white LED spotlight (Advanced Illumination, SL162). The e-jet printer and high-speed camera are synchronized using the drivers of a nanopositioning stage from Aerotech and an automation program, which is written in the Aerotech A3200 Motion Composer Integrated Development Environment.

The substrate used for the experiments is a silicon wafer with 0.005–0.02 Ohm-cm resistivity. The nozzles are pre-pulled glass micropipettes purchased from World Precision Instruments (30 μm inner diameter (DI), 5 cm length (L)) and sputtered with 5 nm gold-palladium to become conductive. The ink material used for the experiments is Norland Optical Adhesive 81 (NOA 81), a UV curable polymer. The material properties that are required to be defined or measured for the model include material density, elongational viscosity, surface tension, relative permittivity, electrical conductivity, and material contact angle with the capillary walls. For NOA 81, these material properties are measured and provided in Table 1.

The nozzle offset from the substrate (standoff height) is 150 μm, and a pulse voltage signal is applied to the nozzle with a high voltage of

Table 1
Material properties of NOA 81.

Material property	Symbol	Value	Unit
Density	ρ	1179	Kg/m^3
Elongational viscosity	μ	972	cP
Surface tension	γ	0.039	N/m
Relative permittivity	ϵ	6.5	1
Electrical conductivity	σ	2.6×10^{-6}	S/m
Contact angle on glass	θ	37	degree

1150 V, a low voltage of 525 V and a pulse width of 2 ms. The camera sample period is 50 μs with a 47 μs exposure time for each frame. The camera lens assembly has a 20 mm working distance and 20× magnification, yielding a spatial resolution of 0.65 μm/pixel. Each frame has a window size of 112 by 272 pixels.

4. Results

4.1. Model validation

Fig. 5 compares the experimental high-speed images with the ink volume fraction simulation results at different time frames demonstrating the e-jet process steps. As can be seen in this figure, the model can capture the critical steps of the e-jet process including build-up, jetting, jet break and Taylor Cone retraction.

The initial condition for the meniscus at low voltage (here, V_l = 525 V) is generally approximated as a spherical cap, illustrated in the high-speed and simulation images. At this part of the process, the electric force is balanced by opposing forces such as the viscous and surface tension forces.

When the voltage is stepped high (here, V_h = 1150 V), electric charge accumulates at the meniscus, creating an electric force in the downward direction. This electric force results in the meniscus deformation from its initial spherical cap shape to a Taylor Cone. As can be seen in Fig. 5, the model captures the Taylor Cone formation "build-up" stage similar to what is observed in the high-speed images. Comparing the high-speed experimental images with the simulation, it can be observed that the Taylor cone forms faster (shorter time duration) within the simulation. There are a number of reasons that could explain some of the discrepan-

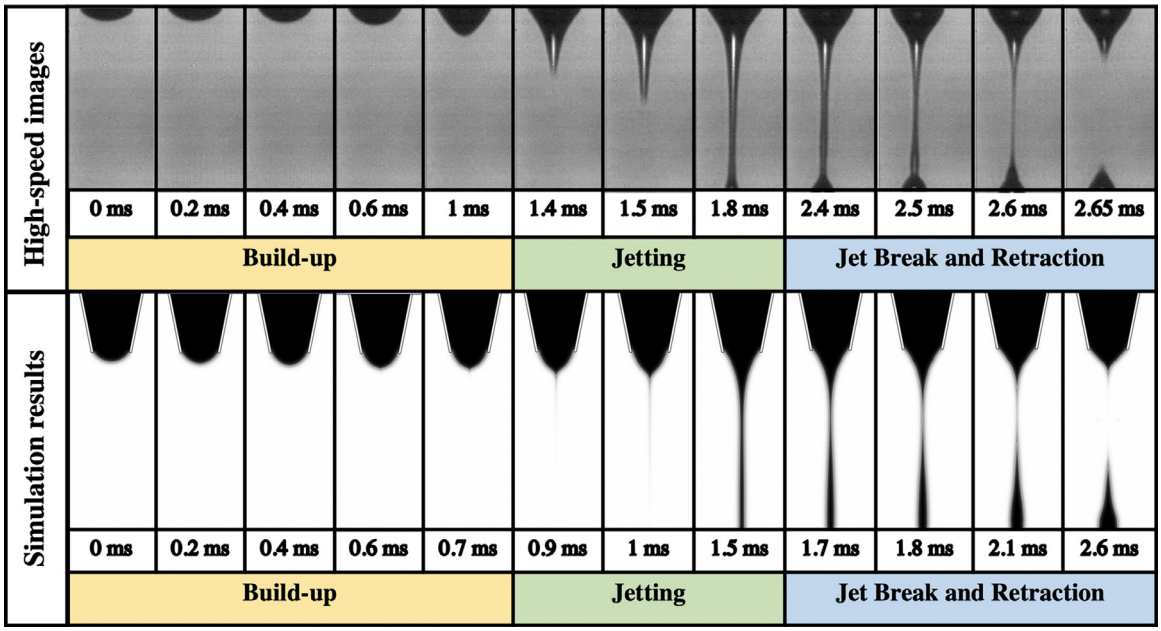

Fig. 5. Model validation. Comparison of high-speed images taken from our experimental setup, and ink volume fraction simulation results for the same setup at different time frames.

cies between the simulation and experimental results: (1) the assumption of a conductive nozzle in the simulation rather than the true set-up that includes a conductive coating (e.g. sputtered gold) that is 10s of nanometers thick applied to a glass nozzle, (2) an instantaneous voltage change applied in simulation while the experimental system exhibits a slew rate of 15 V/μs from the amplifier, and (3) ignoring the interactions between the printed ink and the substrate.

Once the system has been held at the high voltage level for a set period of time (depending on the voltage level and ink material), the electric force will overcome the opposing forces of surface tension and viscous force, and a continuous jet will be generated from the nozzle tip towards the substrate. This stage is called the "jetting" stage. High-speed images from the experiments show significant similarities to the simulation results with a small variation between the onset of the jetting process (0.4 ms and 0.6 ms after the Taylor Cone formation for experiment and simulation, respectively).

As mentioned earlier, the model is capable of capturing the jetting dynamics in the subcritical regime, where the jet is stable during the entire pulse duration. For the experiments, the jet continues until the voltage is stepped down at 2 ms to the low voltage (here, $V_l = 525$ V) and then the jet breaks. Since the build-up process occurs faster for the simulation, the pulse width is selected to be shorter than the experimental setup to ensure that the simulation is conducted in the subcritical regime. Therefore, similar to the experiments, where pulse width is 2 ms for the case of impingement at 1.8 ms, the simulation pulse width is selected to be 11% larger than the impingement time i.e. 1.55 ms since the impingement occurs at 1.4 ms (See Fig. 5). At low voltage, for both the high-speed images and simulation results, it can be seen that the jet thins due to the weakened electric force, which allows the surface tension to dominate the process and break the jet. The jet break takes roughly 0.6 ms after the voltage is stepped down for both the experiments and the model. At this stage, the meniscus retracts back to the nozzle for the simulation, similar to what is observed in the experiments.

Fig. 6 depicts the volume fraction, electric potential, surface tension force, and electric force at the moment that the Taylor Cone is formed (time = 0.8 ms). It can be seen from the electric potential profile that the ink material is at high voltage ($V_h = 1150$ V). The surface tension that is applied to the ink-air interface has a maximum value of roughly 7×10^9 N/m^3 at the apex, where the curvature is sharper than other regions. The electric force at this moment, while a little lower than the surface tension (4×10^9 N/m^3), is trying to overcome the opposing surface tension in order to initiate a jet.

4.2. Sensitivity study of the key parameters

While many states such as velocity, flow rate, and jetting diameter are of interest in e-jet printing, jetting frequency and deposited droplet volume determine the jetting speed and the final printed pattern resolution and are significant outputs of the system to be controlled. Therefore, a sensitivity analysis of some of the key material parameters on the jetting speed and the deposited droplet volume is conducted and presented in this section. The ink material used for these simulations is NOA 81 with a similar setup used for model validation. We conducted a sensitivity analysis on viscosity, surface tension, electrical conductivity and relative permittivity of the material. This investigation provides us with knowledge about the key material parameters and their impact on the e-jet printing process. The simulation is initially run using a step voltage signal to obtain the impingement time, which is provided in Table 2 for each of the case studies. As mentioned previously, this framework is only valid for printing at the subcritical regime, therefore, the pulse width for each case is selected to be 11% longer than the impingement time to ensure that the simulation is conducted in the subcritical regime.

Study I investigates the impact of material viscosity, μ, by holding all material properties and model setup conditions constant and varying the viscosity. Table 2 provides the impingement time and deposited droplet volume for varying viscosity cases: 300 cP, 600 cP, and 972 cP. Larger viscosity values impact the Navier–Stokes equation, contributing to the material resistance to deposition, and therefore a slower jet. As can be seen from the results presented in Table 2, a higher viscosity material will result in a larger viscosity force on the Taylor Cone in the Navier–Stokes equation which will lead to a higher resistance of the ink material to jetting and a smaller volume of ink deposited on the substrate. For a lower viscosity material, we observed that the break occurs at a higher position in the impingement stream, which leads to more material being deposited onto the surface and a larger deposited volume. This observation provides insight into how variability in the printing process can be driven by material properties in the ink, which then lead to changes in achievable droplet resolution for a given material viscosity.

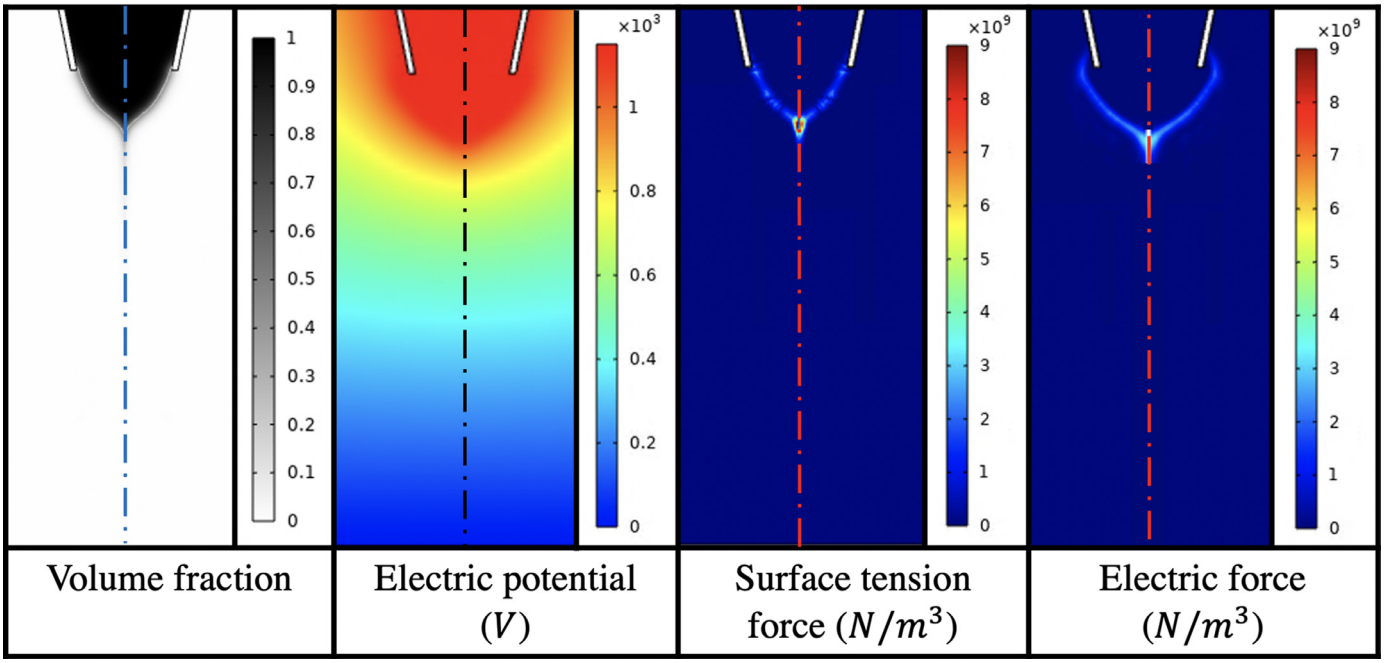

Fig. 6. Plots of volume fraction, surface tension magnitude, electric force magnitude, and velocity at the moment that the Taylor cone is formed (t = 0.8 ms).

Table 2
Sensitivity study parameters.

	Parameters					Model output	
	μ	γ	κ	ϵ	PW	t_{Imp}	v_{drop}
Unit	cP	N/m	S/m	1	ms	ms	pL
	972				1.55	1.4	2.401
Study I	600	0.039	2.6×10^{-6}	6.5	1.11	1	3.374
	300				0.64	0.58	4.919
		0.049			1.85	1.67	1.618
Study II	972	0.039	2.6×10^{-6}	6.5	1.55	1.4	2.401
		0.029			1.36	1.23	4.034
			2.6×10^{-6}		1.55	1.4	2.401
Study III	972	0.039	1×10^{-6}	6.5	1.92	1.73	3.922
			0.5×10^{-6}		2.33	2.1	6.497
				35	1.42	1.28	2.295
Study IV	972	0.039	2.6×10^{-6}	20	1.47	1.33	2.302
				6.5	1.55	1.4	2.401

The parameters μ, γ, κ and ϵ denote viscosity, surface tension, electrical conductivity and relative permittivity, respectively. PW is the voltage pulse width, t_{Imp} is the impingement time and v_{drop} is the deposited droplet volume.

Study II investigates the impact of varying the surface tension coefficient, γ. Studying three different surface tension cases: 0.029 N/m, 0.039 N/m, and 0.049 N/m, we observed that a material with a lower surface tension is governed more by the electric field dynamics, leading to the electric charge at the ink-air interface to be more efficient in its competition with the opposing surface tension force, resulting in a faster jet. This leads to an early initiation of the jetting stage and deposition on the substrate. Note that although the jetting occurs faster for a lower surface tension material, this parameter does not play a significant role in determining the jetting frequency because the jet break happens much slower due to a weaker surface tension force. For instance, for surface tensions of 0.029 N/m and 0.049 N/m, the break occurs at 1.92 ms and 2.01 ms, respectively, while the impingement times are 1.23 ms and 1.67 ms, respectively. In other words, although the impingement time difference for these two cases is 0.43 ms, the jet break occurs with only 0.09 ms difference. Moreover, the simulation results show that the deposited droplet volume is higher for the smaller surface tension coefficient. We hypothesize that this is driven by two things: (1) more material transfer can occur during the early impingement time combined with a later jet break time; (2) the small surface tension in the ink material results in less material being retracted (pulled) back to the nozzle tip. Overall, a smaller surface tension results in a smaller surface tension force on the Taylor Cone in the Navier–Stokes equation resulting in lower resistance to jetting and a larger volume of material deposited on the substrate.

The third study (Study III) investigates the effect of electrical conductivity on the jetting speed and the deposited droplet volume. The electrical conductivity is investigated for three different cases: 2.6×10^{-6} S/m, 1×10^{-6} S/m, and 0.5×10^{-6} S/m. Table 2 shows that for a lower conductive material ($\sigma = 0.5\times10^{-6}$ S/m) jetting happens significantly slower as compared to the more conductive cases (0.7 ms variance). The reason for this difference is that for a lower conductive material, the first term of Eq. (6) becomes small, resulting in a weaker electric force and therefore a slower jet. Furthermore, the simulation results show a decrease in the deposited droplet volume as the electrical conductivity increases. This can be attributed to the fact that a stronger electric force creates a sharper Taylor Cone that can contribute to a finer jet, and therefore less deposited material on the substrate. Snapshots of the simulation volume fraction results for three different cases at the impingement moment are provided in Fig. 7 to demonstrate this phenomenon, which has often been observed in experimental demonstrations and is well documented in the scaling laws literature [21].

The last study (Study IV) considers the impact of relative permittivity of the ink material by varying its value for three different cases: 6.5, 20, and 35. We observed that relative permittivity appears to have a very small effect on the droplet volume. Moreover, we observed that relative permittivity does not greatly impact the jetting speed. Note that jetting speed shows a 0.12 ms faster rate when the relative permittivity is shifted from 6.5 to 35. It should be noted that this specific result only occurs with conductive materials because the coulombic force term in Eq. (6) becomes much larger than the force due to the change in relative permittivity, making the first term dominant and the relative permittivity less effective. In the case of a nonconductive material, the first term in Eq. (6) is zero, and therefore the electric force is generated by the gradient of relative permittivity, leading to the relative permittivity have a much higher impact on the jetting process.

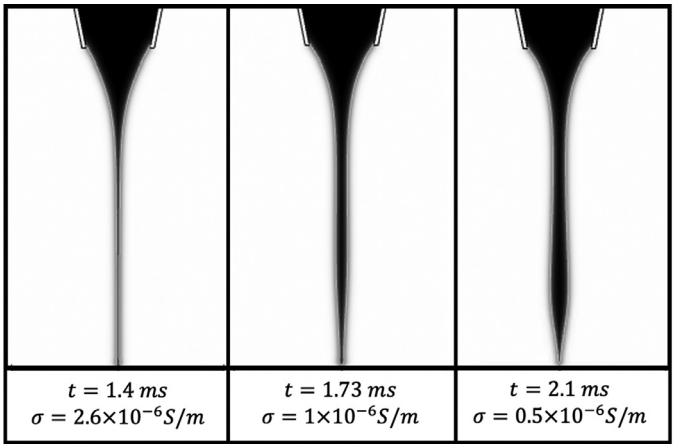

Fig. 7. Plots of volume fraction for three different cases of Study III (varying electrical conductivity, σ) at the impingement moment. The results demonstrate a finer jet for the higher conductivity case.

5. Conclusions

This work presents a framework for high-fidelity modeling of high-resolution electrohydrodynamic jet printing that provides new knowledge from an understanding of the process and the effect of material characteristics on the process dynamics. The model considers an applied pulsed voltage that triggers build up, jetting, jet break, and retraction. The model combines a leaky-dielectric formulation and level set interface tracking method to optimize process parameters for desired material jetting behavior under varying experimental conditions. The model provides the first demonstration of the four critical stages of the jetting process and contributes a platform for identifying critical process and material parameters that can be used to better understand the sensitivity of these parameters to initiate and drive the jetting process. Our studies have shown that material properties, including viscosity, surface tension and electrical conductivity affect the outfeed volume and the jetting frequency significantly.

Simulation results using the model are compared to high-speed images taken from an experimental setup. The results provide the first complete model validation of high-resolution e-jet printing dynamics for a high-fidelity modeling framework. Small discrepancies in timing between the experimental and simulation results are most likely indicative of a lack of interface dynamics between the jet and substrate captured within the model. A series of studies to better understand the effect of material properties on the jetting dynamics were performed.

In the future, the authors will investigate how substrate interactions can be incorporated into the modeling framework. Additionally, the authors will consider methods for extending the use of these models for predicting the printing behavior of different materials as well as towards simplified models for control design.

Declaration of Competing Interest

The authors declare that they have no known competing financial interests or personal relationships that could have appeared to influence the work reported in this paper.

CRediT authorship contribution statement

Nazanin Farjam: Conceptualization, Formal analysis, Validation, Investigation, Methodology, Writing – original draft, Writing – review & editing. **Isaac A. Spiegel:** Formal analysis, Validation, Data curation. **Kira Barton:** Conceptualization, Validation, Supervision, Writing – original draft, Writing – review & editing.

Acknowledgments

This work was supported by the National Science Foundation grant CMMI1727918.

Supplementary material

Supplementary material associated with this article can be found, in the online version, at doi:10.1016/j.mtla.2022.101578

References

[1] T.M. Rodgers, D. Moser, F. Abdeljawad, O.D.U. Jackson, J.D. Carroll, B. H.Jared, D.S. Bolintineanu, J.A. Mitchell, J.D. Madison, Simulation of powder bed metal additive manufacturing microstructures with coupled finite difference-monte carlo method, J. Addit. Manuf. 41 (2021) 101953.
[2] D. D.Phan, J.S. Horner, Z.R. Swain, A.N. Beris, M.E. Mackay, Computational fluid dynamics simulation of the melting process in the fused filament fabrication additive manufacturing technique, J. Addit. Manuf. 33 (2020) 101161.
[3] J. Kattinger, T. Ebinger, R. Kurz, C. Bonten, Numerical simulation of the complex flow during material extrusion in fused filament fabrication, J. Addit. Manuf. 49 (2022) 102476.
[4] J.A. Koepf, M.R. Gotterbarm, M. Markl, C. Körner, 3D multi-layer grain structure simulation of powder bed fusion additive manufacturing, Acta Mater. 152 (2018) 119–126.
[5] L. Lu, N.Sridhar, Y. Zhang, Phase field simulation of powder bed-based additive manufacturing, Acta Mater. 144 (2018) 801–809.
[6] J.P. Delplanque, R.H. Rangel, A comparison of models, numerical simulation, and experimental results in droplet deposition processes, Acta Mater. 46 (1998) 4925–4933.
[7] M.P. Serdeczny, R. Comminal, D.B. Pedersen, J. Spangenberg, Numerical simulations of the mesostructure formation in material extrusion additive manufacturing, J. Addit. Manuf. 28 (2019) 419–429.
[8] J. Park, M. Hardy, S.J. Kang, K. Barton, K. Adair, D. k. Mukhopadhyay, C.Y. Lee, M. Strano, A.G. Alleyne, J.G. Georgiadis, P.M. Ferreira, J.A. Rogers, High-resolution electrohydrodynamic jet printing, Nat. Mater. 6 (2007) 782–789.
[9] N. Farjam, T.H. Cho, N.P. Dasgupta, K. Barton, Subtractive patterning: high-resolution electrohydrodynamic jet printing with solvents, Appl. Phys. Lett. 117 (2020) 133702.
[10] T.H. Cho, N. Farjam, C.R. Allemang, C.P. Pannier, E. Kazyak, C. Huber, M. Rose, O. Trejo, R.L. Peterson, K. Barton, N.P. Dasgupta, Area-selective atomic layer deposition patterned by electrohydrodynamic jet printing for additive manufacturing of functional materials and devices, ACS Nano 14 (2020) 17262–17272.
[11] H. Li, Z. Li, N. Li, X. Zhu, Y. Zhang, L. Sun, R. Wang, J. Zhang, Z. Yang, H. Yi, X. Xu, H. Lan, 3D printed high performance silver mesh for transparent glass heaters through liquid sacrificial substrate electric-field-driven jet, Small 18 (2022) 2107811.
[12] Z. Li, H. Li, X. Zhu, Z. Peng, G. Zhang, J. Yang, F. Wang, Y. Zhang, L. Sun, R. Wang, J. Zhang, Z.Yang, H. Yi, H. Lan, Directly printed embedded metal mesh for flexible transparent electrode via liquid substrate electric-field-driven jet, Adv. Sci. 9 (2022) 2105331.
[13] C.P. Pannier, M. Diagne, I.A. Spiegel, D.J. Hoelzle, K. Barton, A dynamical model of drop spreading in electrohydrodynamic jet printing, J. Manuf. Sci. Eng. 139 (2017) 111008.
[14] G.S. Wright, P.T. Krein, J.C. Chato, Factors affecting dynamic electrical manipulation of menisci, IEEE Trans. Ind. Appl. 29 (1993) 103–112.
[15] J. Yang, H. Kim, B. Cho, J. Chung, Modeling of sessile droplet oscillation on electrohydrodynamic jetting nozzle at constant back pressure, J. Mech. Sci. Technol. 28 (2014) 2815–2823.
[16] I.A. Spiegel, I. Kovalenko, D. Hoelzle, P.M. Sammons, K.L. Barton, Hybrid modeling and identification of jetting dynamics in electrohydrodynamic jet printing, in: 2017 IEEE Conference on Control Technology and Applications (CCTA), 2017.
[17] I.A. Spiegel, P. Sammons, K. Barton, Hybrid modeling of electrohydrodynamic jet printing, IEEE Trans. Control Syst. Technol. 28 (2020) 2322–2335.
[18] C.P. Pannier, M. Wu, D. Hoelzle, K. Barton, A dynamical model of drop spreading in electrohydrodynamic jet printing, in: 2019 American Control Conference (ACC), 2019.
[19] S. An, M.W. Lee, N.Y. Kim, C. Lee, S.S. Al-Deyab, S.C. James, S.S. Yoon, Effect of viscosity, electrical conductivity, and surface tension on direct-current-pulsed drop-on-demand electrohydrodynamic printing frequency, Appl. Phys. Lett. 105 (2014) 214102.
[20] C.H. Chen, D.A. Saville, I.A. Aksay, Scaling laws for pulsed electrohydrodynamic drop formation, Appl. Phys. Lett. 8 (2006) 124103.
[21] H.K. Choi, J. Park, O.O. Park, P.M. Ferreira, J.G. Georgiadis, J.A. Rogers, Scaling laws for jet pulsations associated with high-resolution electrohydrodynamic printing, Appl. Phys. Lett. 92 (2008) 123109.
[22] J.R. Melcher, G.I. Taylor, Electrohydrodynamics: a review of the role of interfacial shear stresses, Annu. Rev. Fluid Mech. 1 (1969) 111–146.
[23] D.A. Saville, Electrohydrodynamics: the Taylor–Melcher leaky dielectric model, Annu. Rev. Fluid Mech. 29 (1997) 27–64.
[24] O. Lastow, W. Balachandranb, Numerical simulation of electrohydrodynamic (EHD) atomization, J. Electrostat. 64 (2006) 850–859.

[25] I. Roghair, M. Musterd, D. van den Ende, C. Kleijn, M. Kreutzer, F. Mugele, A numerical technique to simulate display pixels based on electrowetting, Microfluid Nanofluid 19 (2015) 465–482.
[26] K. Mohammadi, M.R. Movahhedy, S. Khodaygan, A multiphysics model for analysis of droplet formation in electrohydrodynamic 3D printing process, J. Aerosol Sci. 135 (2019) 72–85.
[27] X. Zhao, D. Wang, Y. Lin, Y.Sun, T.Ren, J. Liang, M. Madou, Numerical simulation of coaxial electrohydrodynamic jet and printing nanoscale structures, Microsyst. Technol. 25 (2019) 4651–4661.
[28] Y. Pan, L. Zeng, Simulation and validation of droplet generation process for revealing three design constraints in electrohydrodynamic jet printing, Micromachines 10 (2019).
[29] S.K. Singh, A. Subramanian, Phase-field simulations of electrohydrodynamic jetting for printing nano-to-microscopic constructs, RSC Adv. 10 (2020) 25022.
[30] N. Farjam, I.A. Spiegel, K. Barton, A high-fidelity modeling framework for near-field electrohydrodynamic jet printing, in: Modeling, Estimation and Control Conference (MECC), 2021.